Micromechanical analysis of the development of a yield vertex in polycrystal plasticity

M. Schurig, Berlin, **A. Bertram**, Magdeburg, Germany, **H. Petryk**, Warszawa, Poland

Summary. The Taylor-Lin polycrystal model is used to simulate plastic deformations of a polycrystal. These propagate a corner in the subsequent yield surface due to the intersection of the yield loci of a number of slip mechanisms. Two approaches to identify subsequent yield surfaces and the development of the yield vertex at the applied stress are discussed. A linear regression analysis of the rounded corner is used to identify the corner angle and its development for different strain processes. On deformation paths composed of two aligned segments, the development of a secondary vertex is shown to follow similar laws.

1 Introduction

In crystal plasticity, a number of distinct plastic glide mechanisms contribute simultaneously to the plastic flow. Each one is activated if its critical resolved shear stress is reached and additional loading takes place. For multi-slip, the yield surfaces of the distinct slip systems form a vertex at their intersection [1], forming the multi-faceted crystallite yield locus.

For polycrystals, the number of mechanisms is growing rapidly with the number of grains that interact on the microscale, resulting in the macroscopic plastic flow. However, each slip system of any grain must obey the condition of consistency and thus a vertex results from theoretical considerations at the actual stress point [2].

The effect is an irregular shaped yield locus that has been of particular interest to experimental investigation over many years [3]–[5]. Moreover, due to the interaction of several mechanisms, the direction of plastic flow is not a priori fixed to a single direction, as prescribed by the normality rule applied to a smooth yield surface. Accordingly, there is a transitory range between total loading and total unloading processes [1], [2], [6], [7].

Thus the amount and direction of plastic strain and in the consequence the incremental moduli depend on the direction of the stress rate. Due to the presence of a nonsmooth yield surface, this effect is called *vertex effect* [8]–[12]. This additional incremental nonlinearity is of particular importance for nonproportional processes and connected with the delay effect [13].

Micromechanical models of polycrystals based on crystal plasticity models are nowadays widely used and are able to predict the vertex effect as well as a number of internal structural parameters. However, their solution needs numerical methods that are comparatively costly.

Models that include the vertex effect in phenomenological approaches have been proposed by several authors. Stören and Rice [14] identified the fully active range with the J_2 deformation theory. Christoffersen and Hutchinson [15] introduced a transition function in the partial unloading range between the incremental moduli of fully active and total unloading range. Petryk and Thermann [16], [17] enhanced a two-surface model with a yield vertex and

numerically determined shear bands. Kuroda and Tvergaard used a smooth yield surface but included the vertex effect in their flow rule [10] also for shear band investigations.

Other phenomenological theories of plasticity that incorporate the vertex effect are due to Gotoh [8], Goya and Ito [18], Hu et al. [19], and Tsutsumi and Hashiguchi [12]. The quite general microplane model of plasticity and failure has also been interpreted as a theory with vertex effect by Caner et al. [11].

All these approaches have in common that the transition that describes the nonlinear dependence of the stress rate on the strain rate is the main constituent. Often it is formulated as a function of the outer corner angle at a yield vertex, which is $\frac{\pi}{2}$ for a smooth yield surface. Increased values indicate a more pronounced vertex.

Hutchinson [20] estimated this angle by self-consistent homogenization schemes. In many approaches it is assumed to be constant, at least after an initial phase of vertex development.

In this paper, the development of a vertex during inelastic processes is computed for a whole deformation process, using the classical Taylor-Lin polycrystal model and a viscous grain model (Sect. 2). A large-strain formulation takes texture effects into account. Two distinct indicator functions for the inelastic behavior are used to obtain surrogates for subsequent yield loci and discussed in Sect. 3. In general, the corner angle depends on the deformation history, as the vertex effect is not present in virgin materials. Thus, different standard processes as used, e.g., in [21] are used alone and in two-staged combination in Sect. 4. A linear regression analysis is used for determination of the primary and secondary vertex in such processes.

Recently, Zattarin et al. [22] used a self-consistent scheme to investigate the development of subsequent yield surfaces. They used a different definition of the yield point that prevented the detection of vertices. Accordingly, the corner angle is not subject of their study.

2 The polycrystal model

2.1 The constitutive model for single crystals

The elastic behavior of single crystals is described by a linear law in the undistorted state,

$$\tilde{\mathbf{S}} = \tilde{\mathbb{C}} \left[\frac{1}{2} (\tilde{\mathbf{C}} - \mathbf{1}) \right], \tag{1}$$

using the second Piola-Kirchhoff tensor $\tilde{\mathbf{S}}$ and the right Cauchy-Green tensor $\tilde{\mathbf{C}} = \tilde{\mathbf{F}}^\top \tilde{\mathbf{F}}$. In elastic-plastic behavior, we introduce the unimodular inelastic transformation $\mathbf{P}$, and the elastic transformation $\tilde{\mathbf{F}} = \mathbf{FP}$. According to the concept of isomorphic elastic ranges [23], [24], the elastic law after a plastic deformation can be re-mapped to the reference law Eq. (1) by the isomorphy conditions

$$\mathbf{S} = \mathbf{P} \tilde{\mathbb{C}} \left[\frac{1}{2} (\mathbf{P}^\top \mathbf{CP} - \mathbf{1}) \right] \mathbf{P}^\top,$$

$$\boldsymbol{\tau} = \tilde{\mathbf{F}} \tilde{\mathbb{C}} \left[\frac{1}{2} (\tilde{\mathbf{F}}^\top \mathbf{1} \tilde{\mathbf{F}} - \mathbf{1}) \right] \tilde{\mathbf{F}}^\top. \tag{2}$$

Herein, $\mathbf{S}$ and $\mathbf{C}$ are the second Piola-Kirchhoff stress tensor and the right Cauchy-Green tensor, respectively. $\boldsymbol{\tau} = \mathbf{FSF}^\top$ is the Kirchhoff stress tensor. The latter is completely determined by the elastic transformation. The equivalence to the multiplicative decomposition of the deformation gradient $\mathbf{F}$ is established by the simple identity

$$\mathbf{F} = \tilde{\mathbf{F}}\mathbf{P}^{-1}. \tag{3}$$

Geometrical interpretation of $\tilde{\mathbf{F}}$ as operator between vectors in the undistorted state (lattice vectors) and in the actual placement yields the resolved shear stress in the α-th slip system characterized by the slip system normal $\mathbf{n}^\alpha = \tilde{\mathbf{F}}^{-\top}\tilde{\mathbf{n}}^\alpha$, the slip direction $\mathbf{d}_\alpha = \tilde{\mathbf{F}}\tilde{\mathbf{d}}_\alpha$, and the Schmid tensor $\tilde{\mathbf{M}}_\alpha = \tilde{\mathbf{d}}^\alpha \otimes \tilde{\mathbf{n}}_\alpha$,

$$\tau_\alpha = \mathbf{d}_\alpha \cdot \boldsymbol{\tau}\mathbf{n}^\alpha = \tilde{\mathbf{C}}\tilde{\mathbf{S}} \cdot \tilde{\mathbf{M}}_\alpha. \tag{4}$$

For face-centered cubic metals like copper, the octahedral slip systems are used [25, Table 1].

During elastic processes, $\mathbf{P}$ is constant, while changing according to

$$\mathbf{P}^{-1}\dot{\mathbf{P}} = -\sum_\alpha \dot{\gamma}_\alpha \tilde{\mathbf{M}}_\alpha \tag{5}$$

during inelastic processes. Each slip system contributes an elementary shear at its slip rate $\dot{\gamma}_\alpha$. Here, we use a mildly rate-sensitive nonlinear viscous regularization [26]

$$\dot{\gamma}_\alpha = \dot{\gamma}_0 \left|\frac{\tau_\alpha}{\tau_\alpha^c}\right|^n \operatorname{sign} \tau_\alpha \tag{6}$$

with a power law exponent n and a reference slip rate $\dot{\gamma}_0$. The critical shear stresses τ_α^c are process-dependent hardening variables that require a hardening rule, or in case of perfect plastic material are constant. For the present approach, a viscous flow potential is applied [27],

$$\omega = \frac{1}{n+1}\dot{\gamma}_0 \sum_\alpha \tau_\alpha^c \left|\frac{\tau_\alpha}{\tau_\alpha^c}\right|^{n+1},$$
$$\dot{\gamma}_\alpha = \frac{\partial\omega}{\partial\tau_\alpha}. \tag{7}$$

The evolutions of $\tilde{\mathbf{F}}$ and $\mathbf{F}$ are governed by the spatial velocity gradient $\mathbf{L}$,

$$\dot{\mathbf{F}}\mathbf{F}^{-1} = \mathbf{L},$$
$$\dot{\tilde{\mathbf{F}}}\tilde{\mathbf{F}}^{-1} = \mathbf{L} - \sum_\alpha \dot{\gamma}_\alpha \tilde{\mathbf{F}}\tilde{\mathbf{M}}_\alpha \tilde{\mathbf{F}}^{-1}. \tag{8}$$

2.2 Polycrystal model

As a simple polycrystal model, the fully constrained Taylor-Lin model was used. The localization yields for each grain κ the local velocity gradient from the prescribed global one $\bar{\mathbf{L}}$:

$$\mathbf{L}_\kappa = \bar{\mathbf{L}}. \tag{9}$$

The overall stress is obtained by

$$\bar{\boldsymbol{\tau}} = \frac{1}{N}\sum_\kappa \boldsymbol{\tau}_\kappa. \tag{10}$$

The initial orientations of the grains were chosen to have an initially isotropic aggregate. A total number of $N = 1024$ grains have been optimized for isotropy [28]–[30].

Each of them was modelled using the octahedral slip systems. Material data for copper is summarized in Table 1.

Table 1. Octahedral slip systems [25] (top) and material parameters (bottom)

α	$\tilde{\mathbf{d}}_\alpha$	$\tilde{\mathbf{n}}^\alpha$
1	$(0,1,1)/\sqrt{2}$	$(1,1,-1)/\sqrt{3}$
2	$(1,0,1)/\sqrt{2}$	$(1,1,-1)/\sqrt{3}$
3	$(1,-1,0)/\sqrt{2}$	$(1,1,-1)/\sqrt{3}$
4	$(0,1,-1)/\sqrt{2}$	$(1,-1,-1)/\sqrt{3}$
5	$(1,0,1)/\sqrt{2}$	$(1,-1,-1)/\sqrt{3}$
6	$(1,1,0)/\sqrt{2}$	$(1,-1,-1)/\sqrt{3}$
7	$(0,1,1)/\sqrt{2}$	$(1,-1,1)/\sqrt{3}$
8	$(1,0,-1)/\sqrt{2}$	$(1,-1,1)/\sqrt{3}$
9	$(1,1,0)/\sqrt{2}$	$(1,-1,1)/\sqrt{3}$
10	$(0,1,-1)/\sqrt{2}$	$(1,1,1)/\sqrt{3}$
11	$(1,0,-1)/\sqrt{2}$	$(1,1,1)/\sqrt{3}$
12	$(1,-1,0)/\sqrt{2}$	$(1,1,1)/\sqrt{3}$
γ_0	$1e-3$	
n	80	
τ^c	16.0 MPa	
c_{1111}	168.0 MPa	
c_{1122}	121.4 MPa	
c_{2323}	75.4 MPa	

3 Dissipation and flow potential as indicators of yield

In a strict sense, a single crystal is elastic if all slip rates vanish, $\dot{\gamma}_\alpha = 0$. For the chosen model, this is only the case for vanishing stress. However, for small stresses, the deviation from elasticity is small and can often be neglected.

By the introduction of indicator functions for inelastic behavior we are able to define a critical threshold. The point where it is reached on a radial path defines the boundary of the 'practical' elastic domain.

Dissipation criterion. In [31], based on an inelastic micromechanical simulation, the dissipated power fraction

$$d_\kappa := \frac{\sum_\alpha \tau_\alpha \dot{\gamma}_\alpha}{\tau_\kappa \cdot \mathbf{D}_\kappa} \tag{11}$$

was successfully used. Total elastic behavior is characterized by $\dot{\gamma}_\alpha = 0 \Rightarrow d_\kappa = 0$, while rigid-perfect plastic behavior would lead to total dissipation, the other extremal case $d_\kappa = 1$.

In the present model, a part of the stress power is dissipated (gross effect of dislocation glide), another part is stored (elastic lattice distortion due to external agents and residual stresses on intergranular scale). Residual micro-stresses that would give another, hardening-dependent storage mechanism are not accounted for.

A homogenization of the stress power is possible, and the global dissipation criterion for discrete grains of equal size can be formulated by

$$\bar{d} = \frac{\frac{1}{N}\sum_\kappa \sum_\alpha \tau_\alpha \dot{\gamma}_\alpha}{\bar{\tau} \cdot \bar{\mathbf{D}}}. \tag{12}$$

Figure 1a shows the development of this value during an elastic-plastic tension process. It is constant about 0.8 in spite of hardening, that affects both the dissipated and the total stress power in the same manner. In Fig. 1b, the influence of different prescribed process
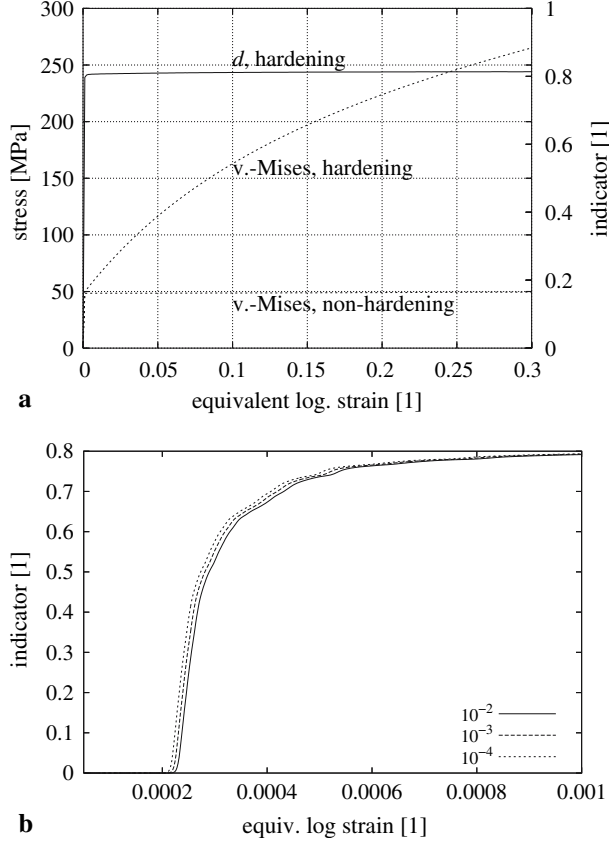
Fig. 1. Stress-strain-curve of a polycrystal: **a** von-Mises equivalent stress in the hardening and non-hardening case, dissipated power fraction $\bar{d}$; **b** Indicator $\bar{d}$ at different strain rates

velocities is shown. A small influence of $\|\mathbf{L}\|$ is visible that does not inhibit the usage as a yield criterion, if the threshold is chosen for a fixed strain rate. Subsequently $\|\mathbf{L}\| = \dot{\gamma}_0$ will always be used [9].

Equation (12) can be used to define a macroscopic elastic domain based on the known inelastic behavior on the micro scale.

Flow potential. Another suitable indicator with a physical background is the viscous flow potential introduced in Eq. (7) [27], [32]. Its transferrability to the macroscale is secured:

$$\bar{\omega} = \frac{1}{\mathcal{B}} \int_{\mathcal{B}} \omega \mathrm{d}V. \tag{13}$$

In contrast to $\bar{d}$, it can be computed from a simple elastic computation. Thus, it does not rely on a microscopic plasticity model (but is of course related to it). It is therefore possible to define a 'practical' elastic domain in a classical manner, i.e., by an indicator function that is a function of stress only at frozen plastic state variables.

In Fig. 2a, out of the virgin state the isoline of the flow potential at $\bar{\omega} = 1$ in the psc-tens (see Table 2 for definition) section of stress space was determined. In addition, radial inelastic processes lead to isolines of the dissipation at $\bar{d} = 25\%$. Both yield comparable curves that approximate Tresca's criterion of maximum shear stress. A rounding of the vertices is obvious, an effect that is stronger for the flow potential.
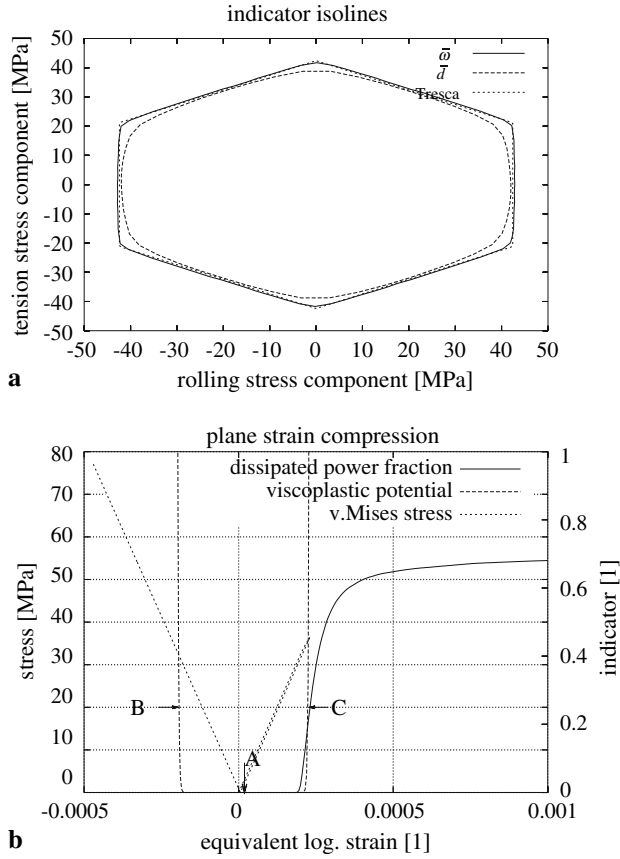
Fig. 2. Flow potential $\bar{\omega}$ and dissipation ratio $\bar{d}$ as indicators of yield

The exact usage of both indicators for the first yield is shown in Fig. 2b. A plane strain compression test with $\bar{\mathbf{L}} = \dot{\gamma}_0 \frac{\mathbf{A}_{\mathrm{psc}}}{\|\mathbf{A}_{\mathrm{psc}}\|}$ was started out of the virgin state. Together with the von Mises equivalent stress, the dissipative power ratio (inelastic process) and the viscous flow potential (elastic process) were plotted.

A 'practically' linear elastic behavior is found up to $\bar{d} = 0.25$ or $\bar{\omega} = 1$ (marked C). At the same time, the dissipation increases massively.

Elastic reversal of the process reveals the plastic proof strain remaining at label A. Unloading can be judged by $\bar{\omega}$ that reaches values as small as 10^{-99}. A value of $\epsilon_{\mathrm{log}} = 2 \times 10^{-5}$ is found. This can be regarded a very strict criterion for the onset of yield, differing orders of magnitude from technical definitions.

It is possible to define even sharper criteria, such as $\bar{\omega} = 10^{-9}$. From Eq. (7) we conclude for only one slip system contributing,

$$\frac{\tau}{\tau^c} = \sqrt[\scriptstyle{[n+1]}]{\frac{N(n+1)}{\dot{\gamma}_0 \tau^c} \bar{\omega}} \approx 0.93, \tag{14}$$

thus $\bar{\omega} = 10^{-9}$ really establishes an approximate criterion for first yield.

Further, the reversed process exhibits a small Bauschinger effect as the critical flow potential is reached in negative direction at a lower stress level (D). This effect has been explained by the residual macrostresses by many authors, e.g., [33], if kinematical hardening is absent.

Indicator Isolines
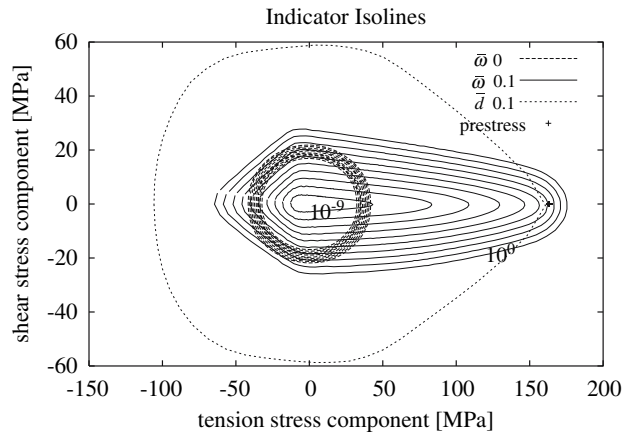
Fig. 3. Initial and subsequent critical surfaces

Subseqent surfaces. For determination of subseqent isosurfaces after a defined prestrain, the same methods were applied. A tens process up to $\epsilon_{\log} = 0.1$ was applied, followed by an unloading process and computation of isolines in the tens-shear stress plane. Figure 3 shows initial and subsequent isolines of the flow potential, for critical values from $\bar{\omega} = 10^{-9}$ by multiples of 10. After prestrain the values reached in prestrain direction vary strongly. $\bar{\omega} = 10^{-3}$ is a suitable indicator for the actual prestrain. Thus a threshold different from the virgin state would be necessary.

In contrast, the plotted dissipation $\bar{d}$ at the same critical value (25% of stress power) lies in close proximity to the stress.

Both indicators clearly exhibit a strong distortion, in particular the formation of a "nose" or rounded vertex. The angle at the outer flanges is similar between the different potential lines, but differs completely from the dissipation line.

4 Corner development at moderate strain

4.1 Identification of corner data

For the identification of the outer corner angle that is regarded as the main descriptive parameter of a yield vertex, the straight parts of the potential isolines have been approximated
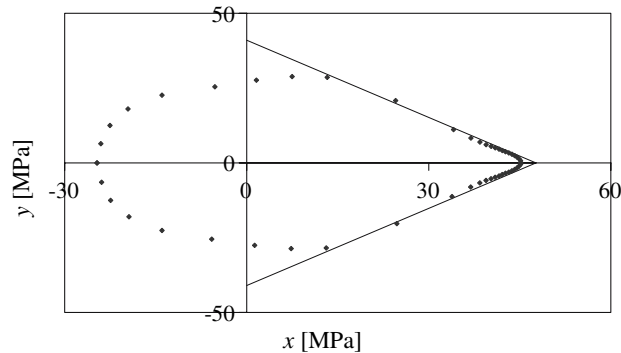
Fig. 4. Identification of the corner by linear regression

by a linear regression (Fig. 4) using two-dimensional coordinates $x = \mathbf{T} \cdot \mathbf{A}_x$ and $y = \mathbf{T} \cdot \mathbf{A}_y$. Note that $\mathbf{A}_x$ and $\mathbf{A}_y$ have not been normalized.

The resulting linear equation in plot sheet coordinates (x, y), $y = m_i x + b_i$, $i = 1, 2$ can be retransferred to the deviatoric Cauchy stress space, using the information which two-dimensional section of stress space is represented by the plot. Thus, lines in the deviatoric stress space according to

$$\mathbf{T}(x) = x \left(\frac{\mathbf{A}_x}{\mathbf{A}_x \cdot \mathbf{A}_x} + m_i \frac{\mathbf{A}_y}{\mathbf{A}_y \cdot \mathbf{A}_y} \right) + b_i \frac{\mathbf{A}_y}{\mathbf{A}_y \cdot \mathbf{A}_y} \tag{15}$$

are generated. Here, $\mathbf{A}_x$ and $\mathbf{A}_y$ denote two of the orthogonal direction tensors as defined in Table 2, or any other pair. Accordingly, the direction of these lines is given by

$$\mathbf{B}_i = \frac{\mathbf{A}_x}{\mathbf{A}_x \cdot \mathbf{A}_x} + m_i \frac{\mathbf{A}_y}{\mathbf{A}_y \cdot \mathbf{A}_y}, \tag{16}$$

and the outer corner angle θ^c (Fig. 5) can be calculated from their full contraction after normalization,

$$\theta^c = \pi - \frac{1}{2} \arccos \frac{\mathbf{B}_1}{\|\mathbf{B}_1\|} \cdot \frac{\mathbf{B}_2}{\|\mathbf{B}_2\|}. \tag{17}$$

The intersection of the two regression lines is at

$$x = \frac{b_2 - b_1}{m_1 - m_2}. \tag{18}$$

Using Eq. (15), the according stress point $\mathbf{T}^c$ can be computed. It is regarded as the idealized vertex if no rounding were present:

$$\mathbf{T}^c = \frac{b_2 - b_1}{m_1 - m_2} \frac{\mathbf{A}_x}{\mathbf{A}_x \cdot \mathbf{A}_x} + \frac{m_1 b_2 - m_2 b_1}{m_1 - m_2} \frac{\mathbf{A}_y}{\mathbf{A}_y \cdot \mathbf{A}_y}. \tag{19}$$

Table 2. Definition of standard processes and process stages

Strain rate tensor	Description
$\begin{bmatrix} 1 & 0 & 0 \\ 0 & -\frac{1}{2} & 0 \\ 0 & 0 & -\frac{1}{2} \end{bmatrix}$	Volume-preserving tension
$\begin{bmatrix} 0 & 1 & 0 \\ 1 & 0 & 0 \\ 0 & 0 & 0 \end{bmatrix}$	Symmetric shear
$\begin{bmatrix} 0 & 0 & 0 \\ 0 & 1 & 0 \\ 0 & 0 & -1 \end{bmatrix}$	Plane strain compression (idealized rolling)

$\epsilon_{\log}$	0	2.5×10^{-4}	4×10^{-4}	6×10^{-4}	1×10^{-3}	2×10^{-3}
Label						A

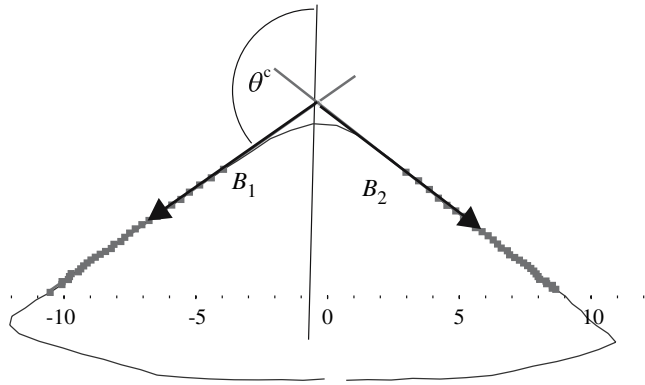| $\epsilon_{\log}$	4×10^{-3}	8×10^{-3}	1.6×10^{-2}	3.2×10^{-2}	1×10^{-1}	
Label				B	C	

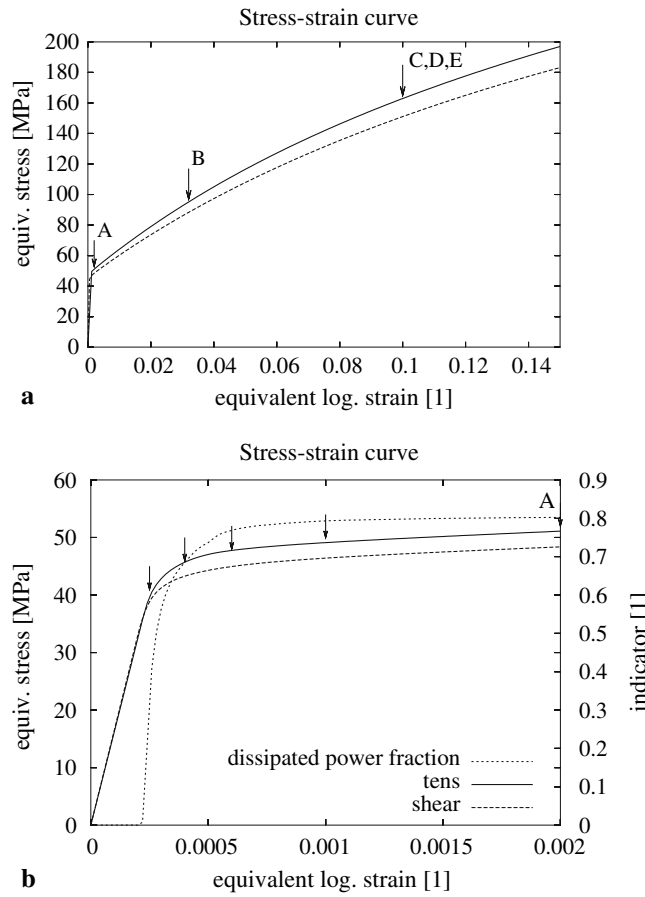**Fig. 5.** Identification of corner angle

Fig. 6. Stress-strain curve and position of sample isolines

4.2 Corner development in volume-preserving tension processes

By application of a tensile prestrain, the equivalent strain finally reached $\epsilon_{eq} = 0.1$ (moderate strain). At different stages in between, elastic unloading and drawing of isolines of the viscous flow potential and the dissipated power in certain sections of stress space was performed. These stages are shown by arrows in Fig. 6. Definitions of process directions and stages are shown in Table 2. Note that symmetric shear and plane strain compression are practically equivalent to each other for an initially isotropic polycrystalline aggregate.
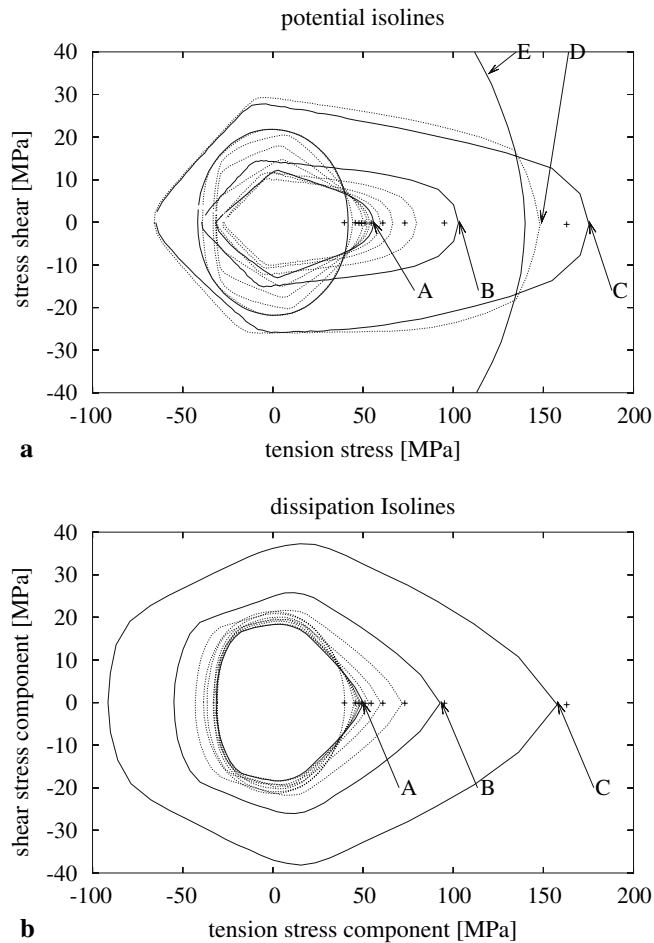
**Fig. 7.** Flow potential and dissipation isolines for different tens prestrains

For $\bar{\omega} = 1$, the result is given in Fig. 7a. In the beginning, a strong distortion of the initially ellipsoidal shape can be seen. In the first subsequent line at a prestrain as small as $\epsilon_{\log} = 2.5 \times 10^{-4}$ at the very onset of plasticity, a rounded nose is already present. The rounding could be minimized by using a smaller critical value.

From the line corresponding to $\epsilon_{\log} = 2 \times 10^{-3}$ (labeled A), after the range of incipient plastic flow, the distortion is not predominant any more. Instead, a nearly self-similar growth takes place.

By the procedure prescribed in Sect. 4, the outer corner angle has been determined. Its development with growing prestrain has been shown in Fig. 8a. One finds saturation-type behavior at an outer corner angle of about $174°$. At stage A, it has already reached $164°$.

Also, for the same stages of a tensile process, the dissipated power was used to produce isolines in Fig. 7b. While the initial isolines are similar in their ellipsoidal shape, there is less distortion of the subsequent lines than in the flow potential plot. In particular, the lateral contraction (negative cross effect) is less pronounced. Also the rounding of the vertex is stronger using the flow potential.

Again, the corner angle has been determined and plotted in Fig. 8b. The resulting angle is smaller at the same prestrain. Saturation cannot be found, but the outer corner angle grows sublinear with prestrain ($\theta^c \propto \log \epsilon^n$, $n < 1$).
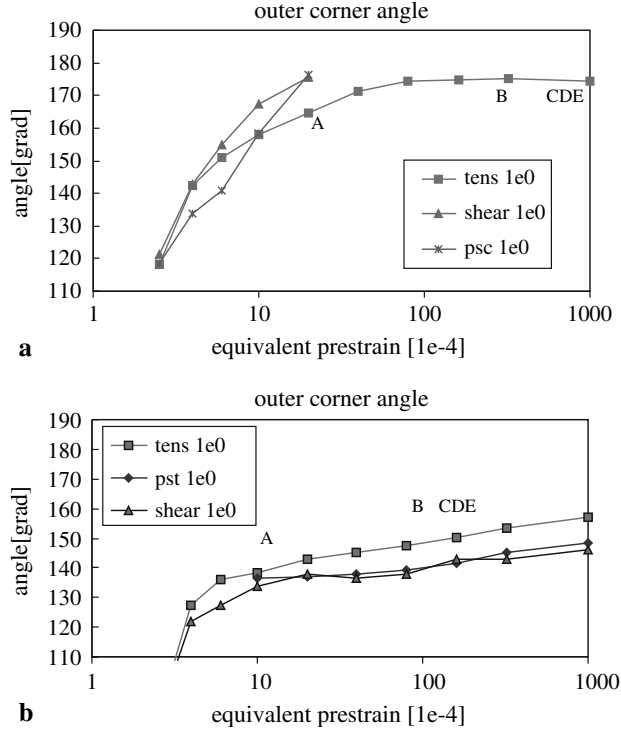
Fig. 8. Development of outer corner angle (**a**) in flow potential (**b**) in dissipation

To explore the differences, the influence of the residual stress and the texture was investigated. Information about both is contained in the statistical distribution of $\tilde{\mathbf{F}}_\kappa$. In a polar decomposition

$$\tilde{\mathbf{F}}_\kappa = \tilde{\mathbf{R}}_\kappa \tilde{\mathbf{U}}_\kappa, \tag{20}$$

$\tilde{\mathbf{R}}_\kappa$ describes the texture information while in a macroscopically unloaded state $\tilde{\mathbf{U}}_\kappa \neq \mathbf{0}$ indicates a residual stress field.

In such a state, replacing $\tilde{\mathbf{F}}_\kappa$ by $\tilde{\mathbf{R}}_\kappa$, the residual stress field has been deleted without changing the texture and hardening information. Then the isolines of the flow potential have been computed once more (Fig. 7a, labeled D). For comparison, the elastic transformations $\tilde{\mathbf{F}}$ have been reset to the initial ones (Fig. 7a, labeled E, large ellipsoid only shown by part.). These are also pure rotations, but this time the initial isotropic texture is represented. It is obvious that the texture information has substantially more influence on the shape of the isoline than the residual stress field.

4.3 Corner development in shear and plane strain compression processes

Shear prestrain processes (see Table 2 for definition) with the defined stages of equivalent strain have been performed in the same manner as in the previous Section. The stress strain-curve is also drawn in Fig. 6. In the plastic range the stress is a little below the tensile process. This reflects the fact that the equivalent strain has been defined based on the Huber-von Mises hypothesis. In fact, the isosurfaces of the virgin polycrystal are between the Huber-von Mises and the Tresca criteria, indicating that shear leads earlier to yield.
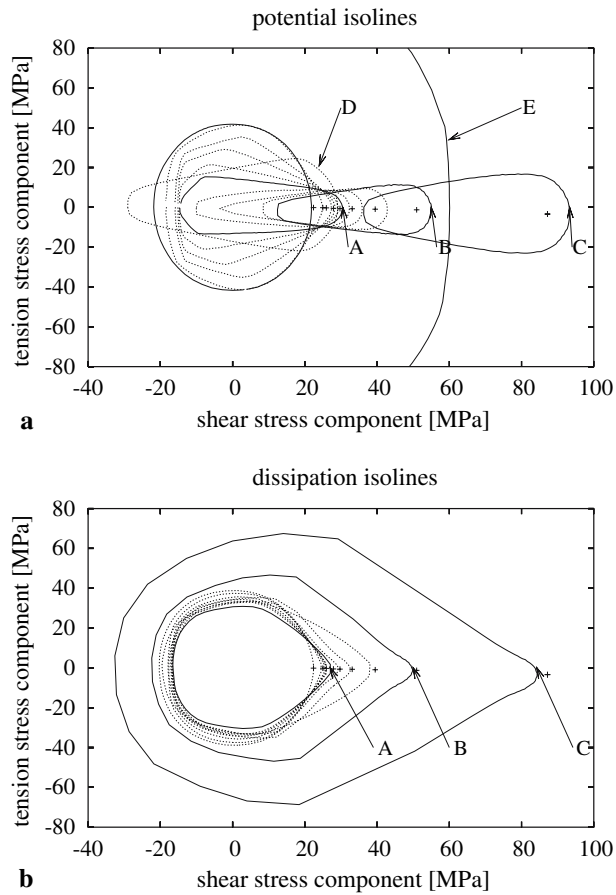
Fig. 9. Flow potential and dissipation isolines for different shear prestrains

Figure 9a shows the development of potential isolines at $\bar{\omega} = 1$ enclosing the prestress points. At an equivalent strain of 2×10^{-3} (Fig. 9a, labeled A) the vertex is well developed. On further stages, the shape of the subsequent isolines degenerates: a strong Bauschinger effect and the distortion makes it impossible to identify a vertex (Fig. 9a, labeled C). In contrast, the dissipation isolines do not exhibit any degeneration. A vertex is clearly identifiable (Fig. 9b).
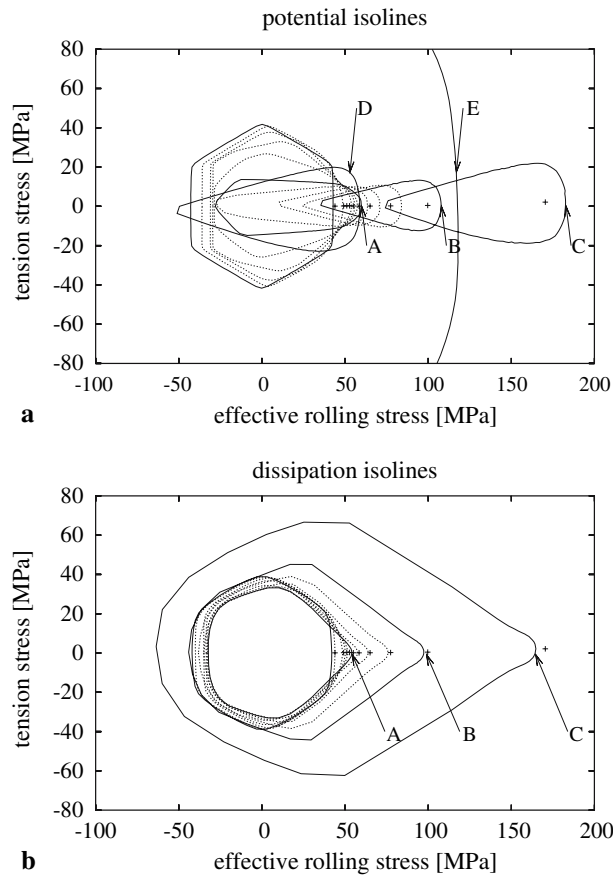
The result of a plane strain compression (idealized rolling) process is similar, Fig. 10.

The elastic transformation $\tilde{\mathbf{F}}_\kappa$ of the single grains has been treated as before to study the origin of this remarkable difference. The deletion of internal stresses in both cases is expressed by a translation of the whole isoline (Fig. 9a, labeled D). If in addition the texture information is reverted to the initial isotropic data (Fig. 9a, labeled E), the distortion of the line vanishes.

This can be explained by non-straight continuation processes.

For the stages of shear prestrain defined in Table 2, elastic continuation processes have been simulated, and the flow potential has been tracked along the process line. For reversed processes, the potential dropped during unloading and eventually reached a minimum before rising again. Similar behavior has been noticed superimposing the reversed strain with some additional straining in an orthogonal direction.

In Fig. 11 the minima of the flow potential have been plotted. Each line visualizes data obtained after a certain level of prestrain. The symbols denote different unloading paths. The lowest minimum is reached for totally reversed processes.

potential isolines

a effective rolling stress [MPa]

dissipation isolines


b effective rolling stress [MPa]

Fig. 10. Flow potential and dissipation isolines for different plane strain compression prestrains
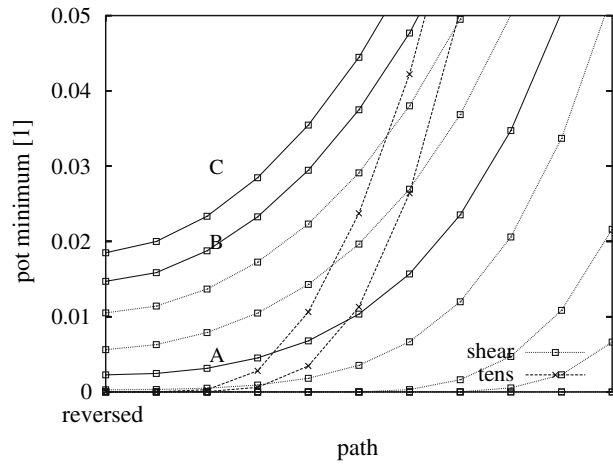
Fig. 11. Minima of flow potential on several continuation processes after previous prestrain stages

While tensile prestrain results in very small minima for totally reversed processes, after shear prestrain it is noticably higher. At stage A, the flow potential does not fall below 1.16×10^{-6} (or 0.2% of its value at a straight continuation). By Eq. (14) this means that at least one slip

potential isolines


a

dissipation isolines

b
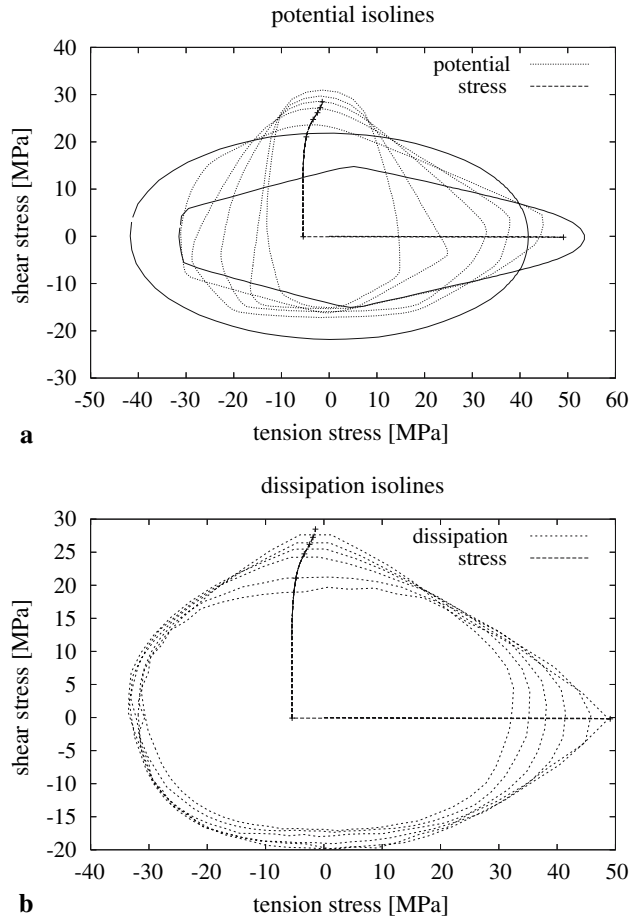
Fig. 12. Isolines at $\bar{\omega} = 1$ for a sequence of tens, unloading and different shear prestrains

system has to be active. Due to the high exponent n in Eq. (6), only few slip systems transitioning the critical stress τ_α^c are sufficient for a strong increase of the flow potential. The inelastic dissipation criterion allows for yield on the according mechanisms, considerably lowering their contribution to $\bar{d}$.

This could be attributed to the residual stress field that is indeed stronger in psc and shear processes. The flow potential is a measure for the resolved shear stress on the most loaded slip systems. A small number of slip systems exceeding the average resolved shear stresses due to the according crystallites residual stress have huge potential influence on the shape of the isoline. By replacement of $\tilde{\mathbf{F}}_\kappa$ by $\tilde{\mathbf{R}}_\kappa$ it has been shown that this is the main source of the translation, but not of the distortion of the isosurface.

An explanation can be given based on the lattice rotation of individual grains. On tens processes, the lattice rotation leads to activation of additional slip systems during rotation towards the stable fibres typical for the drawing texture.

In contrast, on shear and plain strain compression process paths, the set of active slip systems changes frequently, as mechanisms get active and inactive. By reversal of strain it is thus possible that the resolved shear stress in some recently inactivated slip systems approaches the critical value, giving raise to a massively increased flow potential. Hence, already at strain levels of nearly no texture formation, the small lattice rotations combined with the high selectivity of

potential isolines

a

dissipation isolines

b
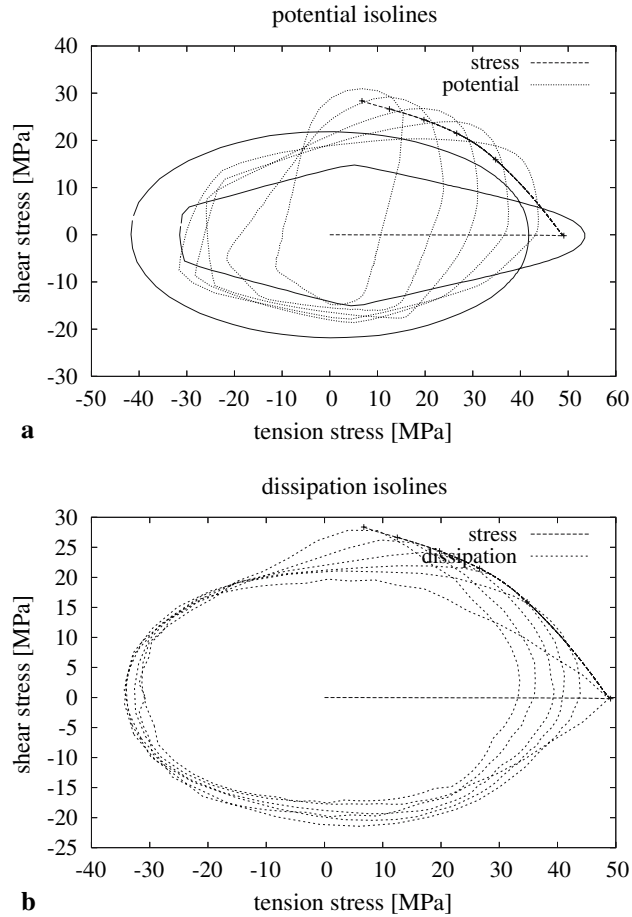
Fig. 13. Isolines at $\bar{\omega} = 1$ for a sequence of tens and different shear prestrains

the flow potential for the first active slip systems lead to excessive distortion of the flow potential isolines. In the dissipation criterion, such slip systems can be filtered out by a threshold being large enough. Such an approach is prevented by the high exponent of the flow potential.

The sharpening of the outer corner angle reaches further stages earlier in shear and psc processes than in tens processes. A similar result has been obtained in the stress-strain curves, once more indicating that the equivalent stress/strain are not perfectly suitable for the model.

4.4 Shear after unloaded tension

A tensile prestrain up to stage A (see Table 2) was followed by an elastic unloading process. From that state, the same program as prescribed above for shear has been performed. Figure 12 shows the resulting potential and dissipation isolines together with the stress path obtained by this sequence.

Near the stress path, a secondary vertex can be found. While it is developing, the prior shape including the primary vertex is dissolved.

The outer corner angle of the secondary vertex has been obtained for a secondary shear of stage A as $135.5°$. In comparison, shear without prior tens process at stage A reaches $138.0°$.
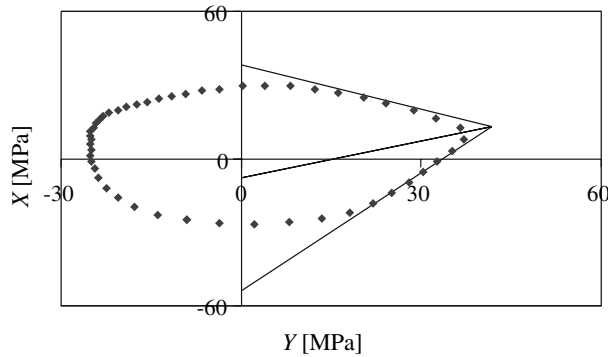
Fig. 14. Linear regression to identify the secondary vertex in the last step of Fig. 13b. Note that the axes have been interchanged.

4.5 Shear immediately after tension

Without intermediate unloading, after tens prestrain up to stage A, strain has been continued by shear processes. Figure 13 shows the resulting potential and dissipation isolines together with the stress path obtained by this sequence. Here, the vertex is not removed but turns along with the actual stress point. The prior shape of the primary vertex has completely transformed (Fig. 14). Here, an outer corner angle of 137.7° is finally reached at stage A.

   The irregular shape makes a regression analysis difficult in the first stages of secondary corner development. Thus, based on the judgement of the outer corner angle reached after additional equivalent accumulated logarithmic strain of $\epsilon_{\log} = 0.001$, the secondary vertex develops like the primary one.

5 Conclusion

Both the viscous flow potential and the dissipated power are suitable indicators for the onset of yield of a virgin material. For the subsequent surfaces after a prestrain, the elastic range at some point has to be replaced by an area of negligible plastic activity. This makes it impossible to use further the viscous flow potential due to its high exponent that inevitably detects the first local and not global yield.

   If the dissipated power is adopted, it is possible to determine the yield vertex that forms near the actual stress point during plastic deformation. The corner angle develops with strain. A saturation of the outer corner angle could not be found, but the growth rate declines strongly. A vertex has already developed at strain levels below typical proof strains of technical definitions of yield.

   If the isotropic equivalent accumulated von-Mises strain is used as a measure of deformation, the growth rate for shear and plane strain compression processes is larger than for tensile processes. This reflects the fact that the initial yield surface is between the Huber-von Mises and the Tresca criteria, and plastic deformation begins at earlier stages of deformation on these processes, too. Thus, a modified equivalent strain could be of advantage.

   On non-linear paths, upon reloading a secondary vertex can be found. Its development occurs after similar amounts of deformation and the outer corner angle is comparable. Also in non-linear paths without unloading, the vertex travels with the direction of applied stress. Thus, the vertex tip and the angle develop coherently, once again similar to the primary vertex.

References

[1] Koiter, W. T.: Stress–strain relations, uniqueness and variational theorems for elastic–plastic materials with a singular yield surface. Q. J. Appl. Math. **11**, 350–354 (1953).

[2] Sanders, J. L. Jr.: Plastic stress–strain relations based on linear loading functions. In: Proceedings of Second U.S. Nat. Congr. Applied Mechanics, pp. 455–460, 1954.

[3] Bertsch, P. K., Findley, W. N.: An experimental study of subsequent yield surfaces–corners, normality, Bauschinger and allied effects. In: Proc. 4th U.S. Nat. Congr. Applied Mechanics 1962.

[4] Hecker, S. S.: Experimental studies of yield phenomena in biaxially loaded metals. In: Constitutive equations in viscoplasticity: computational and engineering aspects (Stricklin, J. A., Saczalski, K. J., eds.), pp 1–34. ASME 1976.

[5] Kuwabara, T., Kuroda, M., Tvergaard, V., Nomura, K.: Use of abrupt strain path change for determining subsequent yield surface: experimental study with metal sheets. Acta Metall. **48**, 2071–2079 (2000).

[6] Batdorf, S. B., Budiansky, B.: A mathematical theory of plasticity based on the concept of slip. NACA Technical Note 1871. Washington: NACA 1949.

[7] Hill, R.: The essential structure of constitutive laws for metal composites and polycrystals. J. Mech. Phys. Solids **15**, 79–95 (1967).

[8] Gotoh, M.: A class of plastic constitutive equations with vertex effect – i. General theory. Int. J. Solids Struct. **21**, 1101–1116 (1985).

[9] Kocks, U. F., Tomé, C. N., Wenk, H. R., eds.: Texture and anisotropy. Cambridge University Press 1998.

[10] Kuroda, M., Tvergaard, V.: Shear band development predicted by a non-normality theory of plasticity and comparisons to crystal plasticity predictions. Int. J. Solids Struct. **38**, 8945–8960 (2001).

[11] Caner, F. C., Bažant, Z. P., Červenka, J.: Vertex effect in strain-softening concrete at rotating principal axes. J. Engng. Mech. **128**, 24–33 (2002).

[12] Tsutsumi, S., Hashiguchi, K.: General non-proportional loading behavior of soils. Int. J. Plast. **21**, 1941–1969 (2005).

[13] Lensky, V. S.: Analysis of plastic behavior of metals under complex loading. In: Plasticity (Lee, E. H., Symonds, P. S., eds.), pp. 259–278. Oxford: Pergamon 1960.

[14] Stören, S., Rice, J. R.: Localized necking in thin sheets. J. Mech. Phys. Solids **23**, 421–441 (1975).

[15] Christoffersen, J., Hutchinson, J. W.: A class of phenomenological corner theories of plasticity. J. Mech. Phys. Solids **27**, 465–487 (1979).

[16] Petryk, H., Thermann, K.: A yield-vertex modification of two-surface models of metal plasticity. Arch. Mech. **49**, 847–863 (1997).

[17] Petryk, H., Thermann, K.: Post-critical plastic deformation in incrementally nonlinear materials. J. Mech. Phys. Solids **50**, 925–954 (2002).

[18] Goya, M., Ito, K.: An expression of elastic-plastic constitutive law incorporating vertex formation and kinematic hardening. ASME J. Appl. Mech. **58**, 617–622 (1991).

[19] Hu, P., Lian, J., Liu, Y. Q., Li, Y. X.: A quasi flow corner theory of elastic–plastic finite deformation. Int. J. Solids Struct. **35**, 1827–1845 (1998).

[20] Hutchinson, J. W.: Elastic–plastic behaviour of polycrystalline metals and composites. Proc. Roy. Soc. Lond. A **319**, 247–272 (1970).

[21] Bronkhorst, C. A., Kalidindi, S. R., Anand, L.: Polycrystal plasticity and the evolution of crystallographic texture in face centered cubic metals. Phil. Trans. R. Soc. Lond. A **341**, 443–477 (1992).

[22] Zattarin, P., Lipinski, P., Rosochowski, A.: Numerical study of the inflence of microstructure on subsequent yield surfaces of polycrystalline materials. Int. J. Mech. Sci. **46**, 1377–1398 (2004).

[23] Bertram, A.: An alternative approach to finite plasticity based on material isomorphisms. Int. J. Plast. **15**, 353–374 (1999).

[24] Bertram, A.: Elasticity and plasticity of large deformations – an introduction. Berlin Heidelberg: Springer 2005.

[25] Kocks, U. F.: The relation between polcrystal deformation and single-crystal deformation. Metall. Trans. **1**, 1121 (1970).

[26] Hutchinson, J. W.: Bounds and self-consistent estimates for creep of polycrystalline materials. Proc. Roy. Soc. Lond. A **348**, 101–127 (1976).

[27] Rice, J. R.: On the structure of stress–strain-relations for time-dependent plastic deformations in metals. J. Appl. Mech. **37**, 728–737 (1970).

[28] Böhlke, T., Bertram, A.: Simulation of texture development and induced anisotropy of polycrystals. In: Proceedings of ICES'98, Modelling and Simulation Based Engineering (Atluri, S., O'Donoghue, P., eds.), pp. 1390–1395, 1998.

[29] Bertram, A., Böhlke, T., Gaffke, N., Heiligers, B., Offinger, R.: On the generation of discrete isotropic orientation distributions for linear elastic cubic crystals. J. Elast. **58**, 233–248 (2001).

[30] Böhlke, T., Bertram, A.: On isotropic orientation distributions of cubic crystals. J. Mech. Phys. Solids **49**, 2459–2470 (2001).

[31] Kraska, M., Bertram, A.: Simulation of polycrystals using an FEM-based representative volume element. Tech. Mech. **16**, 51–62 (1996).

[32] Kiryk, R., Petryk, H.: A self-consistent model of rate-dependent plasticity of polycrystals. Arch. Mech. **50**, 247–263 (1998).

[33] Kraska, M.: Textursimulation bei großen inelastischen Verformungen mit der Technik des repräsentativen Volumenelements (RVE). PhD thesis, TU Berlin, 1998.

Authors' addresses: M. Schurig, Federal Institut for Materials Testing and Research, Unter den Eichen 87, 12205 Berlin, Germany (E-mail: michael.schurig@bam.de); A. Bertram, Otto-von-Guericke-Universität Magdeburg, Germany; H. Petryk, Institute of Fundamental Technological Research, Polish Academy of Sciences, Warszawa, Poland